

Smoothed particle hydrodynamics study of the roughness effect on contact angle and droplet flow

Elena Shigorina,¹ Jannes Kordilla,¹ and Alexandre M. Tartakovsky²

¹*Geoscientific Centre, University of Göttingen, D-37077 Göttingen, Germany*

²*Pacific Northwest National Laboratory, Richland, Washington 99352, USA*

(Received 24 January 2017; revised manuscript received 11 August 2017; published 28 September 2017)

We employ a pairwise force smoothed particle hydrodynamics (PF-SPH) model to simulate sessile and transient droplets on rough hydrophobic and hydrophilic surfaces. PF-SPH allows modeling of free-surface flows without discretizing the air phase, which is achieved by imposing the surface tension and dynamic contact angles with pairwise interaction forces. We use the PF-SPH model to study the effect of surface roughness and microscopic contact angle on the effective contact angle and droplet dynamics. In the first part of this work, we investigate static contact angles of sessile droplets on different types of rough surfaces. We find that the effective static contact angles of Cassie and Wenzel droplets on a rough surface are greater than the corresponding microscale static contact angles. As a result, microscale hydrophobic rough surfaces also show effective hydrophobic behavior. On the other hand, microscale hydrophilic surfaces may be macroscopically hydrophilic or hydrophobic, depending on the type of roughness. We study the dependence of the transition between Cassie and Wenzel states on roughness and droplet size, which can be linked to the critical pressure for the given fluid-substrate combination. We observe good agreement between simulations and theoretical predictions. Finally, we study the impact of the roughness orientation (i.e., an anisotropic roughness) and surface inclination on droplet flow velocities. Simulations show that droplet flow velocities are lower if the surface roughness is oriented perpendicular to the flow direction. If the predominant elements of surface roughness are in alignment with the flow direction, the flow velocities increase compared to smooth surfaces, which can be attributed to the decrease in fluid-solid contact area similar to the lotus effect. We demonstrate that classical linear scaling relationships between Bond and capillary numbers for droplet flow on flat surfaces also hold for flow on rough surfaces.

DOI: [10.1103/PhysRevE.96.033115](https://doi.org/10.1103/PhysRevE.96.033115)

I. INTRODUCTION

Surface roughness and fluid-surface interactions control wettability and flow dynamics of droplets. Droplets are likely to spread on hydrophilic smooth surfaces to form a thin film or puddle and commonly form a spherical shape on fully hydrophobic smooth surfaces when droplet sizes are comparable to the capillary length of water [1]. A surface is considered hydrophobic if the static contact angle is larger than 90° and hydrophilic, otherwise. On smooth surfaces, the static contact angle θ_0 only depends on the fluid-solid molecular interactions. Therefore, in this paper, we will refer to this as the microscopic contact angle θ_0 . On rough surfaces, the static contact angle, which we call the effective contact angle θ_{eff} , depends on both the fluid-solid molecular interactions (and θ_0) and surface roughness. Various authors have experimentally investigated the dependence of the contact angles on the chemical composition and roughness of solid surfaces [e.g., 2–4]. Recently, molecular dynamics (MD) simulations have been used to study the effect of nanoscale roughness on static contact angles of droplets [5,6]. It was shown that smooth hydrophilic surfaces can become less hydrophilic if certain types of roughness are added. In some cases, a superhydrophobic rough surface with a contact angle of 180° can be created.

Droplet flow on rough surfaces has been investigated experimentally and numerically using MD simulations by Huang *et al.* [7], Byun *et al.* [8], Zhang *et al.* [9], and Stamatopoulos *et al.* [10]. For example, Zhang *et al.* [9] experimentally studied the droplet velocities on grooved surfaces with various inclination angles and different orientations of grooves relative to the flow direction. Results indicated that droplets experience less resistance to flow if grooves are oriented parallel to the

flow direction, and they move significantly faster. On the other hand, water droplets barely moved when the grooves were oriented perpendicular to the flow direction.

In this work, we investigate contact angle dynamics of sessile and transient droplets on rough hydrophobic and hydrophilic surfaces using the pairwise force smoothed particle hydrodynamics (PF-SPH) method implemented in LAMMPS [11], a massively parallel library for particle simulations. In PF-SPH, the boundary conditions at the fluid-fluid and fluid-fluid-solid interfaces are modeled by pairwise forces [12]. In contrast to other numerical methods for multiphase flows [e.g., 7], PF-SPH allows for discretizing only the liquid phase in liquid-gas flows, which significantly reduces the computational cost for modeling water droplet flows where most of the domain usually is occupied by air.

A validation of the PF-SPH method for fluid-fluid systems (where both fluids are explicitly modeled) for modeling fluid-fluid and fluid-fluid-solid interfaces, including dynamic contact angles, with respect to Young-Laplace [13] and Tanner [14] laws was presented in Tartakovsky and Panchenko [12]. Similarly, here, we demonstrate the accuracy of PF-SPH for liquid-gas systems where only the liquid phase is explicitly modeled. Furthermore, the model is shown to reproduce the Cassie-to-Wenzel transition based on critical capillary pressure and internal droplet pressure. Next, we use the PF-SPH model to simulate highly intermittent, gravity-driven free-surface flows for a diverse range of wetting conditions on time and length scales that are inaccessible to MD. We also use the PF-SPH method to study the effect of roughness on the effective static contact angle. We construct four surface geometries to investigate the changes of static contact angles of sessile droplets: rectangular, dual-rectangular, sinusoidal, and dual-sinusoidal surfaces.

Similar to the experimental work of Zhang *et al.* [9], we study the effect of surface roughness orientation relative to the flow direction on the motion of water droplets and observe good qualitative agreement with our simulations. Grooves oriented parallel to the flow direction result in higher droplet velocities, while they impede movement when oriented perpendicular to the flow direction. We cast our results in a dimensionless form to investigate the relationship between Bond (Bo) and capillary (Ca) numbers for different surface inclination angles and types of roughness. Simulations show that linear scaling relationships between Bo and Ca numbers for droplet flow on smooth surfaces [15] also hold on rough surfaces.

II. GOVERNING EQUATIONS AND PF-SPH METHOD

We consider flow of water and air phases, where the air phase is continuous. Under this condition, it is common to disregard the effect of the air phase on water flow and model the latter by a combination of the continuity equation,

$$\frac{d\rho}{dt} = -\rho \nabla \cdot \mathbf{v}, \quad (1)$$

and the momentum conservation equation,

$$\frac{d\mathbf{v}}{dt} = -\frac{1}{\rho} \nabla P + \frac{\mu}{\rho} \nabla^2 \mathbf{v} + \mathbf{g}, \quad (2)$$

subject to the free-surface boundary condition at the fluid-air interface,

$$-P\mathbf{n} = -\tau \cdot \mathbf{n} + \kappa\sigma\mathbf{n}, \quad (3)$$

and a no-slip boundary condition at the fluid-solid boundary. Here, $\tau = [\mu(\nabla\mathbf{v} + \nabla\mathbf{v}^T)]$ is the viscous stress tensor, \mathbf{v} the velocity, P is the pressure, μ is the viscosity, \mathbf{g} is the gravitational acceleration, κ is the interface curvature, σ is the surface tension, and the normal vector \mathbf{n} points away from the nonwetting phase. In addition, the microscopic contact angle needs to be specified at the water-air-solid contact line.

In this work, we use the weakly compressible PF-SPH method [16,17] to solve Eqs. (1)–(3). SPH is a mesh-free Lagrangian method where fluids are discretized with a set of N points, commonly referred to as *particles*. Each particle is defined by its position \mathbf{r}_i , mass m_i , density ρ_i , and velocity \mathbf{v}_i , $i = 1, \dots, N$. SPH is based on the approximation of a continuous function and its derivative:

$$f(\mathbf{r}) = \sum_j^N \frac{m_j}{\rho_j} f(\mathbf{r}_j) W(|\mathbf{r} - \mathbf{r}_j|, h), \quad (4)$$

$$\nabla f(\mathbf{r}) = \sum_j^N \frac{m_j}{\rho_j} f(\mathbf{r}_j) \nabla W(|\mathbf{r} - \mathbf{r}_j|, h), \quad (5)$$

where the kernel $W(|\mathbf{r} - \mathbf{r}_j|, h)$ satisfies the normalization condition,

$$\int W(|\mathbf{r} - \mathbf{r}_j|, h) d\mathbf{r} = 1, \quad (6)$$

and has compact support h . In the limit of $h \rightarrow 0$, W approaches the Dirac delta function $\delta(|\mathbf{r} - \mathbf{r}_j|)$:

$$\lim_{h \rightarrow 0} W(|\mathbf{r} - \mathbf{r}_j|, h) = \delta(|\mathbf{r} - \mathbf{r}_j|). \quad (7)$$

A number of functional forms of W have been used in the literature. Here, we use W in the form of a so-called “Wendland” kernel [18]:

$$W = \alpha_k \begin{cases} \left(1 - \frac{|\mathbf{r}|}{h}\right)^3 & \text{if } 0 \leq |\mathbf{r}| < h \\ 0 & \text{if } |\mathbf{r}| \geq h, \end{cases} \quad (8)$$

where $\alpha_k = 168/16\pi h^3$.

The PF-SPH discretization of Eqs. (2) and (3) is

$$\begin{aligned} \frac{d\mathbf{v}_i}{dt} = & -\sum_{j=1}^N m_j \left(\frac{P_j}{\rho_j^2} + \frac{P_i}{\rho_i^2} \right) \frac{\mathbf{r}_{ij}}{r_{ij}} \cdot \frac{dW(r_{ij}, h)}{dr_{ij}} \\ & + 2\mu \sum_{j=1}^N m_j \frac{\mathbf{v}_{ij}}{\rho_i \rho_j r_{ij}} \cdot \frac{dW(r_{ij}, h)}{dr_{ij}} + \mathbf{g} + \frac{1}{m_i} \sum_{j=1}^N \mathbf{F}_{ij}. \end{aligned} \quad (9)$$

The particle positions are advanced according to

$$\frac{d\mathbf{r}_i}{dt} = \mathbf{v}_i. \quad (10)$$

The particle-particle interaction force \mathbf{F}_{ij} in Eq. (9) is used to generate surface tension and the fluid wetting behavior. Here, we use \mathbf{F}_{ij} in the form

$$\mathbf{F}_{ij} = s_{ij} \left[A_{ij} \tilde{W} \left(r_{ij}, \frac{h}{2} \right) \frac{\mathbf{r}_{ij}}{r_{ij}} - \tilde{W}(r_{ij}, h) \frac{\mathbf{r}_{ij}}{r_{ij}} \right], \quad (11)$$

where \tilde{W} is a cubic spline function:

$$\tilde{W}(r_{ij}, h) = \begin{cases} 1 - \frac{3}{2} \left(\frac{r}{h} \right)^2 + \frac{3}{4} \left(\frac{r}{h} \right)^3 & \text{if } 0 \leq \frac{r}{h} < 0.5 \\ \frac{1}{4} \left(2 - \frac{r}{h} \right)^3 & \text{if } 0.5 \leq \frac{r}{h} < 1 \\ 0 & \text{if } \frac{r}{h} \geq 1 \end{cases} \quad (12)$$

and s_{ij} and A_{ij} are parameters determining the magnitude of surface tension and the microscopic static contact angle. To impose the no-slip boundary condition away from the fluid-fluid-solid contact line and the contact angle at the contact line, the solid phase is discretized with a set of static “solid” particles, and summation in Eq. (9) is performed over both fluid and solid particles. The parameter s_{ij} is set to s_{ff} when particle j is a fluid particle and s_{sf} when particle j is a solid particle [particle i in Eq. (9) is always a fluid particle]. For a liquid to wet a surface, s_{ff} should be set greater than s_{sf} and vice versa. In this work, the parameter A_{ij} is set to $A_{ff} = 8$ for interactions between two fluid particles and to $A_{sf} = 24$ for interactions between fluid and solid particles.

The density is obtained from kernel summation as

$$\rho_i = \sum_{j=1}^N m_j W(\mathbf{r}_{ij}, h). \quad (13)$$

To evaluate pressure at each time step, we employ an equation of state (EOS) following Batchelor [19] and Monaghan [20]:

$$P = P_0 \left\{ \left(\frac{\rho}{\rho_0} \right)^\gamma - 1 \right\}, \quad (14)$$

where

$$P_0 = \frac{c^2 \rho_0}{\gamma}. \quad (15)$$

Here, ρ_0 is the reference water density and $\gamma = 3$ and the speed of sound c are chosen so that the relative density fluctuation $|\delta\rho|/\rho$ is small enough (less than 3%) to approximate an incompressible fluid [21]. To integrate Eq. (9), we employ a modified velocity Verlet time stepping scheme:

$$(1) \mathbf{v}_i(t + \frac{1}{2}\Delta t) = \mathbf{v}_i + \frac{1}{2}\mathbf{a}_i(t); \quad (16a)$$

$$(2) \bar{\mathbf{v}}_i(t + \Delta t) = \mathbf{v}_i(t) + \Delta t \mathbf{a}_i; \quad (16b)$$

$$(3) \mathbf{r}_i(t + \Delta t) = \mathbf{r}_i(t) + \Delta t \mathbf{v}_i(t + \frac{1}{2}\Delta t); \quad (16c)$$

(4) calculation of $\mathbf{a}_i(t + \Delta t)$ using extrapolated velocity $\bar{\mathbf{v}}_i$;

$$(5) \mathbf{v}_i(t + \Delta t) = \mathbf{v}_i(t + \frac{1}{2}\Delta t) + \frac{1}{2}\mathbf{a}_i(t + \Delta t), \quad (16d)$$

where $\mathbf{a}_i = \frac{\mathbf{f}_i}{m_i}$ is the acceleration.

Time step constraints are given by Tartakovsky and Meakin [16]:

$$\Delta t \leq 0.25h/3c, \quad (17a)$$

$$\Delta t \leq 0.25 \min(h/3|\mathbf{a}_i|)^{1/2}, \quad (17b)$$

$$\Delta t \leq \min(\rho_i h^2/9\mu_i), \quad (17c)$$

where $|\mathbf{a}_i|$ is the magnitude of acceleration \mathbf{a}_i .

In our simulations, we set the density and viscosity of water to $\rho_0 = 1000 \text{ kg/m}^3$ and $\mu = 0.001296 \text{ Pa s}$, respectively. Initially, the SPH particles are placed on a uniform cubic lattice with the lattice size $0.5 \times 10^{-4} \text{ m}$ (unless mentioned otherwise), which results in a fluid particle mass of $m_0 = 1.25 \times 10^{-10} \text{ kg}$. The mass of solid particles is set to that of the fluid particle. The smoothing length is set to $h = 1.71 \times 10^{-4} \text{ m}$, the speed of sound to $c = 4.5 \text{ ms}^{-1}$, and the gravitational acceleration to $\mathbf{g} = 9.81 \text{ m/s}^2$.

III. MODEL PARAMETRIZATION AND VERIFICATION

A. Surface tension

The parameter s_{ff} is calibrated with respect to the surface tension of water by simulating a droplet and using the Young-Laplace law to relate the difference of pressure inside and outside of the bubble, ΔP and its radius, R_{eq} , to the surface tension σ :

$$\sigma = \frac{R_{\text{eq}}}{2} \Delta P. \quad (18)$$

Because the pressure outside of the bubble is zero, ΔP is equal to the pressure inside the bubble. It should be noted that the total pressure in PF-SPH is a sum of the pressure prescribed via the EOS and generated by \mathbf{F}_{ij} . As in any particle system, the total pressure generated by SPH particles can be calculated from the virial formula [16,17,22,23]:

$$P_T = \frac{1}{2dV_r} \sum_i \sum_j \mathbf{r}_{ij} \mathbf{f}_{ij} = \frac{1}{8r_v^3} \sum_i \sum_j \mathbf{r}_{ij} \mathbf{f}_{ij}, \quad (19)$$

where $d = 3$ for a three-dimensional system and $\sum_j \mathbf{f}_{ij} = m_i d\mathbf{v}_i/dt$. The double summation is performed over all particles within the distance r_v from the droplet center, where

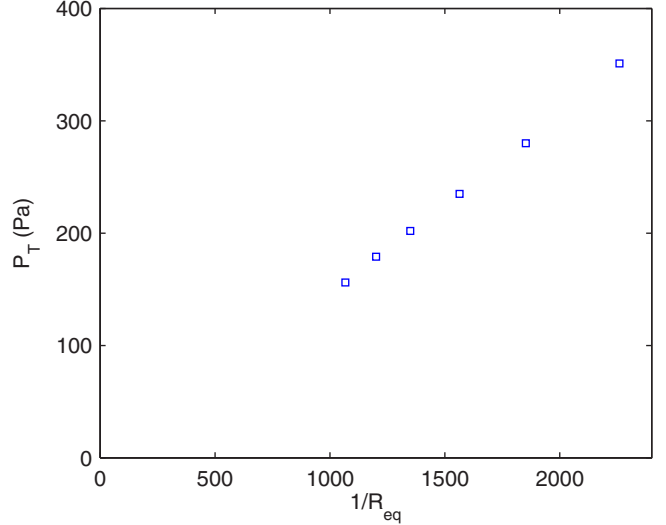


FIG. 1. Pressure for various droplet sizes.

$r_v = R_{\text{eq}} - h$, to exclude the boundary deficiency effect. We obtain the surface tension of water with $s_{\text{ff}} = 3.5 \times 10^{-6}$. Six liquid droplets with radii ranging from 0.5 to 1 mm are simulated in the absence of gravity with $s_{\text{ff}} = 3.5 \times 10^{-6}$ and the other parameters as described. Figure 1 shows the fluid pressure P_T in the center of the equilibrated liquid droplet versus $1/R_{\text{eq}}$. The surface tension, found as half of the slope of the straight line fitted through the simulation results, is $\sigma = 73.14 \text{ mN m}^{-1}$ (the water surface tension is 72 mN m^{-1} at 25 C).

B. Static contact angles on smooth surface

To measure static contact angles, we simulate droplets that are slowly brought into contact with the flat surface. Each droplet has a volume of $V = 2.14 \text{ mm}^3$. After droplets reach equilibrium and remain static, we select fluid particles at the intersection of the droplet surface with the xy and zy planes and fit circles with radius R_x in the xy plane and R_z in the zy plane as shown in Fig. 2. The contact angles θ_0^x in the x direction and θ_0^z in the z direction can be found as

$$\theta_0^{x,z} = 90 \pm \arcsin\left(\frac{l_{x,z}}{R_{x,z}}\right), \quad (20)$$

where $l_{x,z}$ is a distance between circle center and solid surface. In Eq. (20), the addition is carried out for static contact angles larger than 90° and subtraction otherwise. The static contact angle θ_0 is equal to the arithmetic mean of θ_0^x and θ_0^z .

For the parameter set described above, the (microscopic) static contact angle θ_0 on a smooth surface depends on the interaction forces s_{sf} between solid and fluid particles (Table I). Figure 3 shows that θ_0 decreases with increasing s_{sf} . All static contact angles θ_0 are measured with a standard error $SE_{\bar{\theta}_0} \approx \pm 0.2^\circ$, which is computed as

$$SE_{\bar{\theta}_0} = \frac{s}{\sqrt{n}}, \quad (21)$$

where s is the standard deviation of the mean $\bar{\theta}_0$ of $n = 5$ droplets. Droplets are brought into contact with the solid

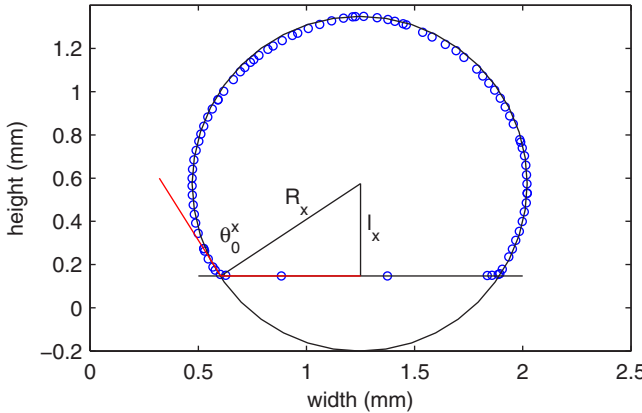


FIG. 2. Static contact angle measurements. Here, only the droplet cross section in the xy plane is shown.

surface from five different distances in order to randomize the dynamic contact line movement until a static contact angle is achieved.

To investigate the pinning effect due to the discrete nature of the solid surface we compute the difference ε_0 in contact angles in the x and z directions:

$$\varepsilon_0 = |\theta_0^x - \theta_0^z|. \quad (22)$$

The values of ε_0 are reported in Table I. In these simulations ε_0 is less than 1° , and we assume that pinning effects are negligible for the chosen resolution.

To validate our model, we simulate droplet spreading on a horizontal surface [Fig. 4 (inset)] and compare the time-dependent height of the droplet, H , with the Tanner law: $H \sim t^{-2n/3}$, where $n = 0.3$ in three spatial dimensions [14]. The simulation is initialized by placing a droplet with an initial radius $R_0 = 1.2$ mm on the horizontal surface. After equilibration of the droplet on the solid surface in the presence of gravity, we prescribe a solid-fluid interaction force of $s_{sf} = 3 \times 10^{-6}$ and measure the height changes of the droplet over time.

Figure 4 shows H as a function of time obtained from the simulation with the exponent $n = 0.274$, which is close to the theoretical value of $n = 0.3$.

C. Dynamic contact angles on smooth surface

Here we demonstrate that the PF-SPH model predicts dynamic contact angles in accordance with the theoretical Cox-Voinov relationship [13,24]. The dynamic contact angle

TABLE I. Static contact angles of droplets for different solid-fluid interaction strengths s_{sf} .

s_{sf}	0	1×10^{-6}	1.3×10^{-6}	1.8×10^{-6}	2.2×10^{-6}	2.8×10^{-6}
θ_0^x	122.4°	100.8°	85.2°	81.3°	77.2°	0.1°
θ_0^z	122.9°	101.2°	84.3°	81.7°	77.7°	72.2°
θ_0	122.7°	100.9°	84.7°	81.5°	77.5°	72.8°
ε_0	0.5°	0.4°	0.9°	0.4°	0.5°	0.8°

as a function of the contact line velocity is measured by simulating a plate withdrawal from a pool of liquid. According to the Cox-Voinov relationship, the receding contact angle scales with the capillary number, Ca , as

$$\theta_0^3 - \theta_r^3 \sim Ca, \quad (23)$$

where Ca is defined as

$$Ca = \mu \frac{v}{\sigma}, \quad (24)$$

and v is the velocity of the moving plate.

The simulation setup is shown in Fig. 5 (inset). The receding angle is computed as the angle formed by a circle, fitted to the interface, and the solid boundary. From Fig. 5 we find that $\theta_0^3 - \theta_r^3 \sim Ca^\alpha$ with $\alpha = 0.9469$, which is close to the theoretical value $\alpha = 1$.

Physically, θ_0 depends on the chemical composition of fluids and the solid surface, and, numerically (in the PF-SPH model), θ_0 is a function of the interaction parameters s_{sf} and s_{ff} . Therefore, we refer to θ_0 as a *microscopic static contact angle*. In the following, we study droplet behavior on rough surfaces obtained by “carving” a flat surface and characterize macroscopic wetting properties of these rough surfaces in terms of the effective contact angle formed by a droplet and a plane fitted to the rough surface.

IV. WENZEL AND CASSIE DROPLETS ON ROUGH SOLID SURFACES

Depending on θ_0 and surface roughness, a droplet on a rough surface can be in one of the three regimes: the Wenzel regime [25], the Cassie regime [26], or the mixed Cassie-Wenzel regime. Figure 6 shows the PF-SPH simulations of a droplet in all three regimes. On “microscopically” hydrophilic rough surfaces (i.e., surfaces with $\theta_0 > \pi/2$), Wenzel drops are formed by the fluid filling surface indentations [Fig. 6 (middle)]. On microscopically hydrophobic surfaces, depending on the ratio of roughness to the size and mass of the

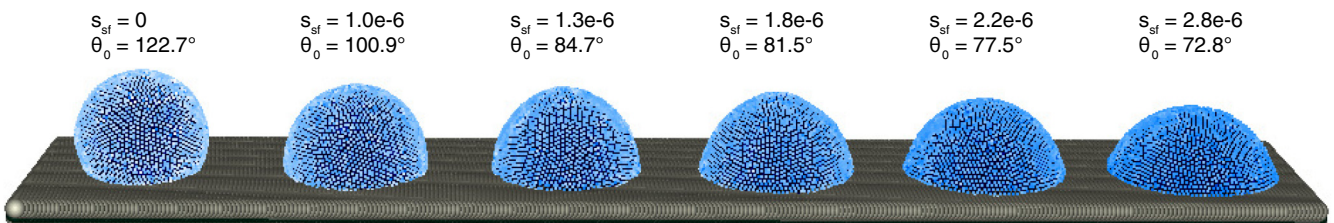


FIG. 3. Static contact angles for different solid-fluid interaction strengths s_{sf} .

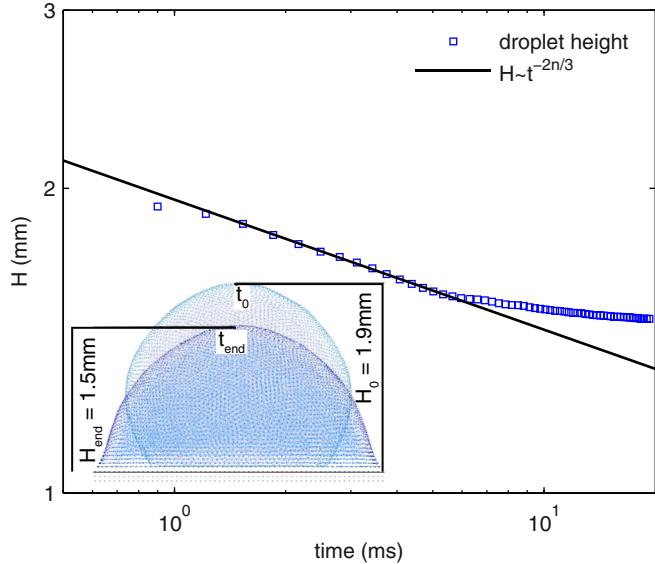


FIG. 4. Model verification with respect to Tanner's law: height of the droplet as a function of time. The inset shows the droplet spreading on a horizontal surface.

droplet, Cassie [Fig. 6 (left)] or Cassie-Wenzel regime [Fig. 6 (right)] droplets can form. In the Cassie regime, a droplet “rests” on the surface spikes, while a droplet partially filling the pits and depressions of a rough surface is considered to be in the Cassie-Wenzel regime. In general, the effective contact angle θ_{eff} , formed by a droplet on a rough surface, differs from the microscopic static contact angle θ_0 .

In the following, we simulate droplets in all three regimes and study the relationship between the roughness geometry, θ_0 (or the parameter s_{sf}), and θ_{eff} . We investigate both hydrophobic surfaces ($\theta_0 > 90^\circ$) and hydrophilic ($\theta_0 < 90^\circ$) surfaces.

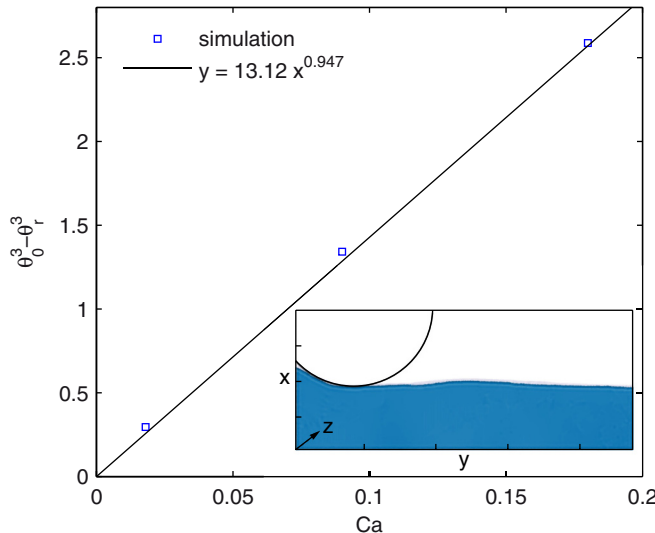


FIG. 5. Cox-Voinov relationship for receding contact angles. The inset shows the simulation results of a plate withdrawal from a pool of liquid ($x = 25$ mm, $y = 10$ mm).

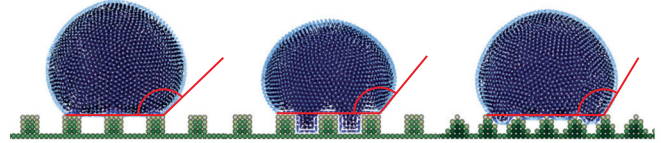


FIG. 6. Different states of droplets depending on wetting conditions (left to right): Cassie state, Wenzel state, and Cassie-Wenzel state.

V. EFFECTIVE CONTACT ANGLES OF DROPLETS ON ROUGH MICROSCOPICALLY HYDROPHOBIC SURFACES

Microscopically hydrophobic rough surfaces are modeled by setting $s_{\text{sf}} = 0$, which yields $\theta_0 = 122.7^\circ$. We consider four types of rough surfaces with rectangular, dual-rectangular, sinusoidal, and dual-sinusoidal patterns (see Fig. 7).

We model droplets with an initial radius $R = 0.8$ mm, which are slowly brought into contact with a rough surface. After equilibration of a droplet on the rough surface, we measure the effective contact angle θ_{eff} in the x and z directions as shown in Fig. 2. For Wenzel and Cassie-Wenzel droplets, which penetrate depressions of the rough surface, we measure θ_{eff} relative to the nominal smooth surface on top of the blocks, as indicated in Figs. 6 (middle) and 6 (right) by the solid line. Depending on their geometry, solid surfaces are discretized with approximately 20 000 boundary particles and droplets with 17 075 fluid particles. Simulations are run on eight processors.

A. Rectangular and dual-rectangular surfaces

Figure 7 (first from left) shows the rectangular-patterned surface. This surface is parametrized by the distance d between “bars,” the height H , and the width l of the bars. We study three rectangular-patterned surfaces with different parameters l and d , and $H = 0.2$ mm: a fine-roughness surface with small d and l [Fig. 8(a)], a medium-roughness surface [Fig. 8(b)], and a coarse-roughness surface with large d and l [Fig. 8(c)].

Figure 7 (second from left) depicts the dual-rectangular surface. It is constructed of blocks of height H , length l , and the distance d between the blocks. Figures 8(d)–8(f) show three types of dual-rectangular surfaces: a fine-roughness surface [Fig. 8(d)], a medium-roughness surface [Fig. 8(e)], and a coarse-roughness dual-rectangular surface [Fig. 8(f)].

Figure 8 also shows the equilibrated droplets on rectangular-patterned surfaces. Table II provides the corresponding effective contact angle values. The effective static contact angle θ_{eff}^x measured in the x direction perpendicular to the bars increases with decreasing l and/or increasing d . All droplets on hydrophobic rectangular surfaces are in a Cassie state. The effective static contact angle θ_{eff}^z of a droplet measured in the z direction parallel to the ripples varies between 123.3° and 125.5° , which is close to the corresponding $\theta_0 = 122.7^\circ$.

Due to the isotropic geometry of the dual-rectangular-patterned surfaces, θ_{eff}^x and θ_{eff}^z are the same in both directions [Figs. 8(d)–8(f)]. The largest contact angle $\theta_{\text{eff}}^x \approx \theta_{\text{eff}}^z \approx 151^\circ$ is measured on a fine dual-rectangular surface [Fig. 8(d)]. In contrast, the droplets on medium- and coarse-roughness

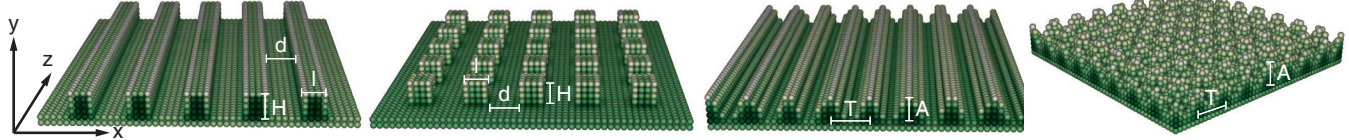


FIG. 7. Surface parameters (four types, from left to right): (1) for rectangular surface—height H and width l of a bar; d —distance between bars; (2) for dual-rectangular surface—height H and l width of a block; d —distance between blocks; (3) for sinusoidal surface—period T and magnitude A of a sinusoidal function in the x direction; (4) for dual-sinusoidal surface—period T and magnitude A of a sinusoidal function in the x and z directions.

surfaces are in the Wenzel state, even though not all small surface depressions are completely filled with fluid because of microscale surface hydrophobicity. The effective contact angles of “Wenzel” droplets are larger than the microscopic static contact angle, and the microscale hydrophobic rough surfaces also show macroscale hydrophobic behavior.

B. Sinusoidal and dual-sinusoidal surfaces

Here, we study the contact angles of droplets on sinusoidal surfaces with longitudinal ripples in the z direction and a sinusoidal cross section in the x direction [Fig. 7 (third from left)]. The sinusoidal surfaces are parametrized as

$$S(x,z) = \frac{A}{2} \cos\left(x \frac{2\pi}{T}\right) + 0.00015, \quad (25)$$

and the solid boundary in simulations is constructed by filling the region $y < S(x)$ with solid particles. The parameters of this surface are the period of the sinusoidal function T and the magnitude A in the y direction, which is equal for all types of sinusoidal surfaces $A = 0.2$ mm. We employ three types of rough sinusoidal surfaces: a fine-roughness surface with

$T = 0.2$ mm [Fig. 9(a)], a medium-roughness surface with $T = 0.25$ mm [Fig. 9(b)], and a coarse-roughness sinusoidal surface with $T = 0.3$ mm [Fig. 9(c)].

The dual-sinusoidal surface is created as a surface with sinusoidal cross sections in the x and z directions [Fig. 7 (fourth from left)], described by the equation

$$S(x,z) = \frac{A}{2} \cos\left(x \frac{2\pi}{T}\right) + \frac{A}{2} \cos\left(z \frac{2\pi}{T}\right) + 0.00015. \quad (26)$$

The parameter T is varied to create three surfaces: a fine-roughness surface with $T = 0.2$ mm [Fig. 9(d)], a medium-roughness surface with $T = 0.25$ mm [Fig. 9(e)], and a coarse-roughness dual-sinusoidal surface with $T = 0.3$ mm [Fig. 9(f)]. The magnitude A is equal to 0.2 mm for all three surfaces. In the simulations, the region $y < S(x,z)$ is filled with solid particles.

Figure 9 depicts droplets on the sinusoidal and dual-sinusoidal surfaces and Table II shows the effective static contact angles. Here, the droplet on the fine sinusoidal surface is in the Cassie state, the droplet on the medium sinusoidal surface is in the Cassie-Wenzel state, and droplets on the coarse sinusoidal and dual-sinusoidal surfaces are macroscopically

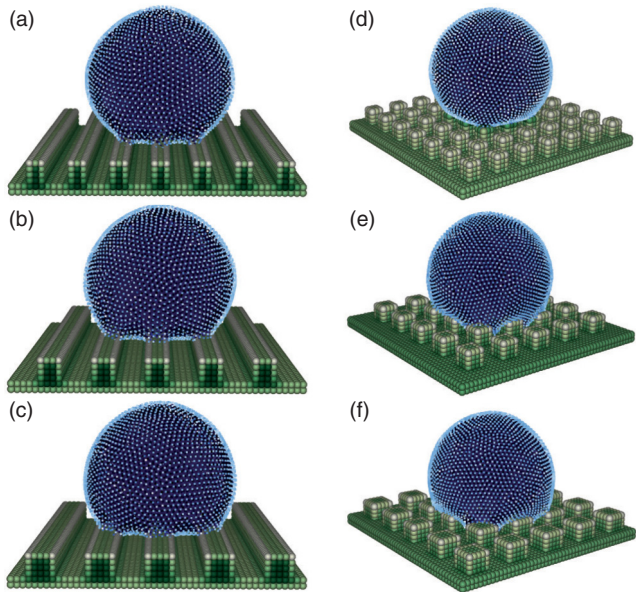


FIG. 8. Static contact angles of droplets on hydrophobic rectangular [(a)–(c)] and dual-rectangular [(d)–(f)] surfaces. Surface parameters are $d = 0.2$ mm, $l = 0.15$ mm [(a), (d)]; $d = 0.25$ mm, $l = 0.2$ mm [(b), (e)]; $d = 0.25$ mm, $l = 0.25$ mm [(c), (f)]; $H = 0.2$ mm for all types of surfaces.

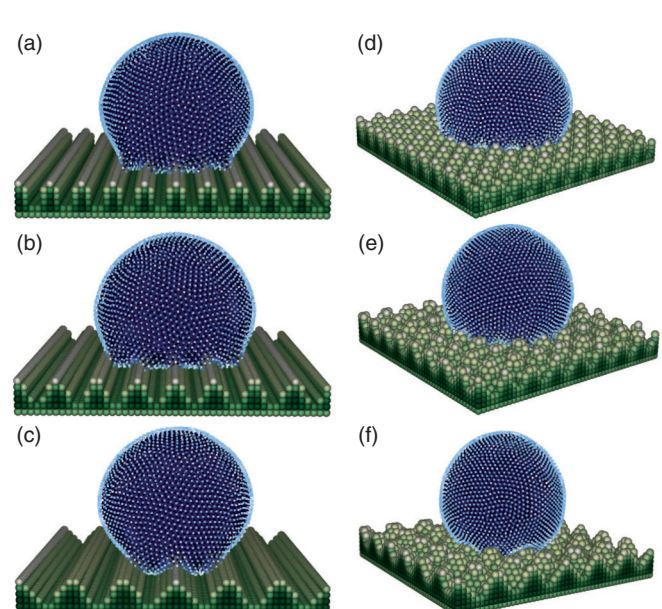


FIG. 9. Static contact angles of droplets on hydrophobic sinusoidal [(a)–(c)] and dual-sinusoidal [(d)–(f)] surfaces. Surface parameters are $A = 0.2$ mm, $T = 0.2$ mm [(a), (d)]; $A = 0.2$ mm, $T = 0.25$ mm [(b), (e)]; $A = 0.2$ mm, $T = 0.3$ mm [(c), (f)].

TABLE II. Effective static contact angles of droplets on rough hydrophobic and hydrophilic surfaces. fr: fine roughness; mr: medium roughness; cr: coarse roughness.

	Rectangular			Dual-rectangular			Sinusoidal			Dual-sinusoidal		
λ	0.0469 (fr)	0.0781 (mr)	0.0977 (cr)	0.0469 (fr)	0.0781 (mr)	0.0977 (cr)	0.0625 (fr)	0.0781 (mr)	0.0938 (cr)	0.0625 (fr)	0.0781 (mr)	0.0938 (cr)
Hydrophobic surfaces												
Hydrophilic surfaces												
θ_{eff}^x	152.9°	142.7°	130.3°	151.5°	135.5°	125.9°	144.6°	128.3°	145.3°	111.8°	121.2°	135.7°
θ_{eff}^z	123.3°	124.6°	125.5°	150.6°	136.6°	128.1°	106.7°	110.5°	118.4°	110.5°	122.9°	135.7°
ε_{eff}	29.6°	18.1°	4.8°	0.9°	1.1°	2.2°	37.9°	17.8°	26.9°	1.3°	1.7°	0°
θ_{eff}^x	103.7°	129.2°	122.2°	98.1°	94.5°	96.5°	99.8°	117.6°	123.2°	105.4°	113.7°	95.7°
θ_{eff}^z	80.9°	81.1°	84.7°	95.7°	94.5°	100.6°	74.6°	72.9°	79.7°	103°	114.5°	96.5°
ε_{eff}	22.8°	48.1°	37.5°	2.4°	0°	4.1°	25.2°	44.7°	43.5°	2.4°	1.2°	0.8°

in the Wenzel state. For all considered microscopically hydrophobic rough surfaces, the effective static contact angle is greater than 90°, i.e., these surfaces are macroscopically hydrophobic.

VI. EFFECTIVE CONTACT ANGLES OF DROPLETS ON ROUGH MICROSCOPICALLY HYDROPHILIC SURFACES

The microscopic hydrophilic behavior of droplets on a solid surface is achieved by setting the solid-fluid interaction strength to $s_{sf} = 1.3 \times 10^{-6}$, which yields $\theta_0 = 84.7^\circ$. The surface geometries are the same as in the preceding section (see Fig. 7). We find that Wenzel droplets form on all considered microscopically hydrophilic surfaces (see Figs. 10 and 11).

Table II lists the resulting effective contact angles. The effective static contact angle of Wenzel droplets on the dual-rectangular and dual-sinusoidal microscopically hydrophilic surfaces are larger than 90°. This means that the dual-

rectangular and dual-sinusoidal roughnesses considered in this work make microscopically hydrophilic surfaces macroscopically hydrophobic. For the rectangular-rough and sinusoidal-rough surfaces, the effective contact angles in the x direction are greater than 90°, but the effective contact angles in the z direction are smaller than the corresponding microscopic contact angle. These types of surfaces have mixed effective wettability, i.e., they are macroscopically hydrophilic in the z direction and hydrophobic in the x direction.

VII. DIMENSIONLESS ANALYSIS OF EFFECTIVE STATIC CONTACT ANGLES

The influence of surface geometry on the effective contact angles of droplets can be described by the (dimensionless) scaling ratio λ . For rectangular and dual-rectangular surfaces, the scaling ratio λ is defined as

$$\lambda = \frac{ld}{R_0^2}, \quad (27)$$

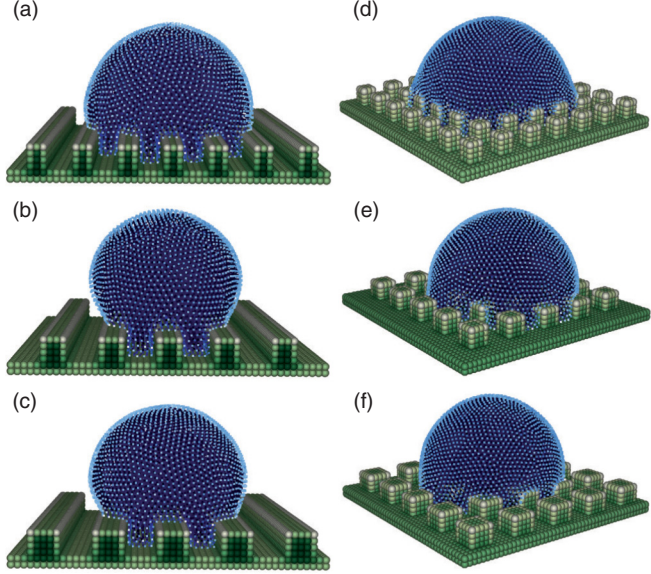


FIG. 10. Static contact angles of droplets on hydrophilic rectangular [(a)-(c)] and dual-rectangular [(d)-(f)] surfaces. Surface parameters are $d = 0.2$ mm, $l = 0.15$ mm [(a), (d)]; $d = 0.25$ mm, $l = 0.2$ mm [(b), (e)]; $d = 0.25$ mm, $l = 0.25$ mm [(c), (f)]; $H = 0.2$ mm for all types of surfaces.

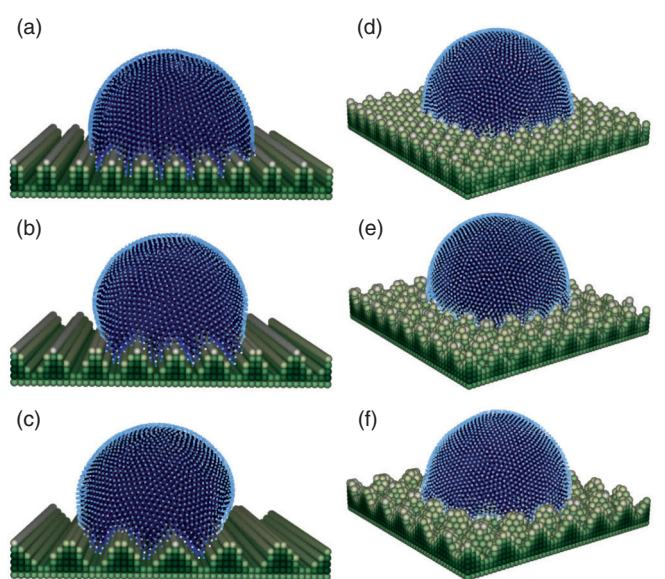


FIG. 11. Static contact angles of droplets on hydrophilic sinusoidal [(a)-(c)] and dual-sinusoidal [(d)-(f)] surfaces. Surface parameters are $A = 0.2$ mm, $T = 0.2$ mm [(a), (d)]; $A = 0.2$ mm, $T = 0.25$ mm [(b), (e)]; $A = 0.2$ mm, $T = 0.3$ mm [(c), (f)].

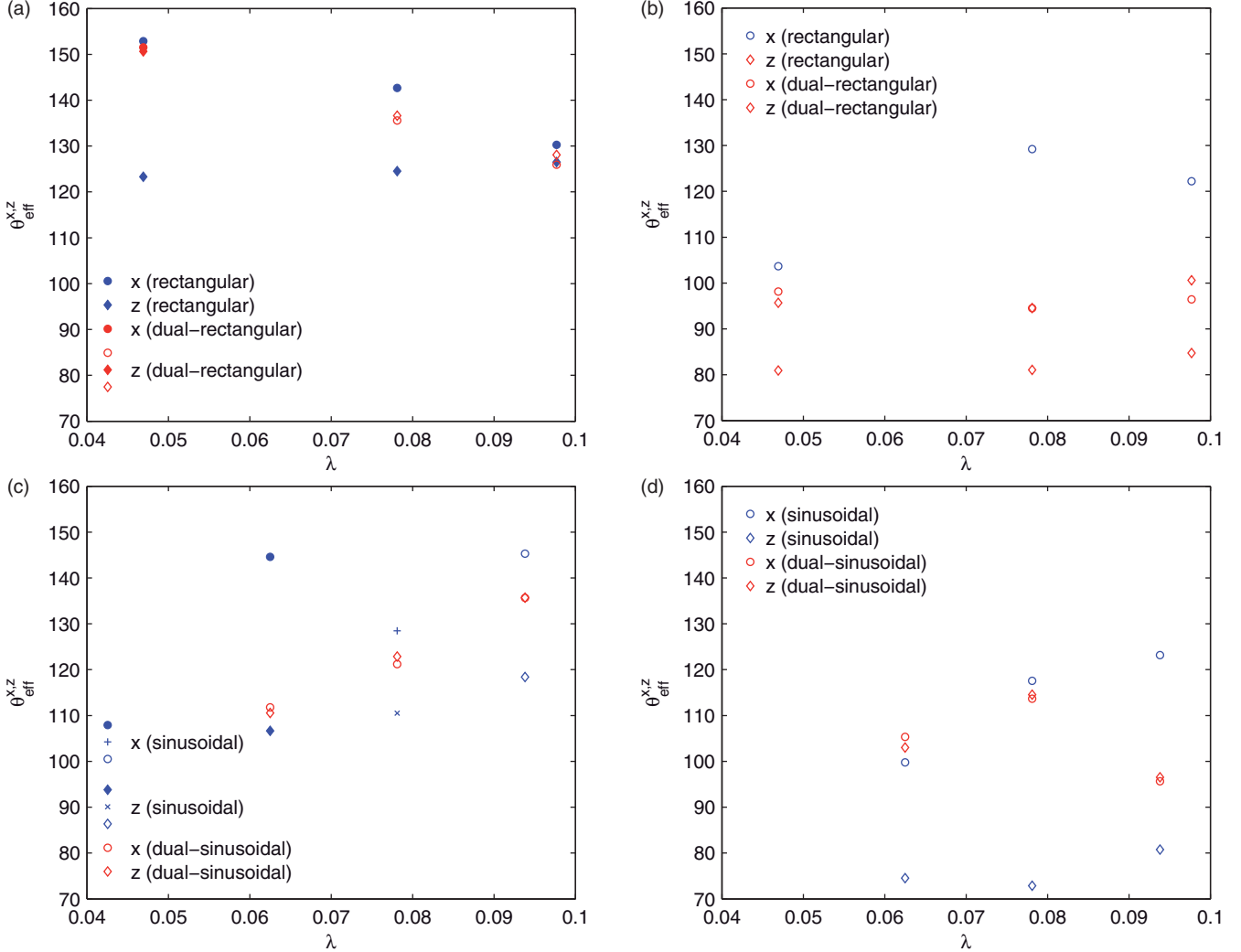


FIG. 12. Effective static contact angles θ_{eff}^x and θ_{eff}^z for scaling ratio λ between 3.5×10^{-3} and 8.5×10^{-3} for hydrophobic rectangular and dual-rectangular (a), hydrophilic rectangular and dual-rectangular (b), hydrophobic sinusoidal and dual-sinusoidal (c), and hydrophilic sinusoidal and dual-sinusoidal (d) surfaces. Solid symbols represent droplets in a Cassie state, and open symbols represent droplets in a Wenzel state. Symbols “plus” and “cross” represent a droplet in a Cassie-Wenzel state.

and for sinusoidal and dual-sinusoidal surfaces as

$$\lambda = \frac{AT}{R_0^2}, \quad (28)$$

where l , d , A , and T are the surface parameters and R_0 is an initial droplet radius. Table II lists the effective static contact angles of droplets, modeled in previous sections, with respect to λ . All angles are measured with $SE_{\theta_0} \approx \pm 0.2^\circ$.

Figure 12 shows the relationship between λ and effective static contact angles, θ_{eff}^x and θ_{eff}^z , of droplets on hydrophobic and hydrophilic rough surfaces. The dependence of θ_{eff}^x and θ_{eff}^z on λ is different for Wenzel and Cassie droplets. The effective contact angles of Cassie droplets decrease with increasing λ . The effective contact angles of Wenzel droplets may increase or decrease with increasing λ , depending on the type of surface geometry. For example, for hydrophilic dual-rectangular surfaces, the effective contact angles do not change significantly with λ [Fig. 12(c)], while for other types of surfaces, θ_{eff} may increase or decrease with increasing λ .

The largest effective contact angles are achieved by Cassie droplets on hydrophobic dual-rectangular surfaces, and the smallest effective contact angles are reached by Wenzel droplets on hydrophilic sinusoidal and dual-sinusoidal surfaces. The angle θ_{eff}^z on the rectangular hydrophobic and hydrophilic surfaces is close to the corresponding θ_0 , while θ_{eff}^z of sinusoidal hydrophobic and hydrophilic surfaces is smaller than θ_0 . For all other considered surfaces, θ_{eff}^x and θ_{eff}^z are larger than the corresponding θ_0 .

We quantify the directional dependence of the effective static contact angle by ε_{eff} , the difference between θ_{eff}^x and θ_{eff}^z of each droplet:

$$\varepsilon_{\text{eff}} = |\theta_{\text{eff}}^x - \theta_{\text{eff}}^z|. \quad (29)$$

We report ε_{eff} in Table II and Fig. 13 for all studied values of λ . For dual-rectangular and dual-sinusoidal hydrophobic and hydrophilic surfaces ε_{eff} is less than 5° , while for rectangular and sinusoidal hydrophobic and hydrophilic surfaces ε_{eff} varies in the range from 5° to 50° . Droplets on rectangular and

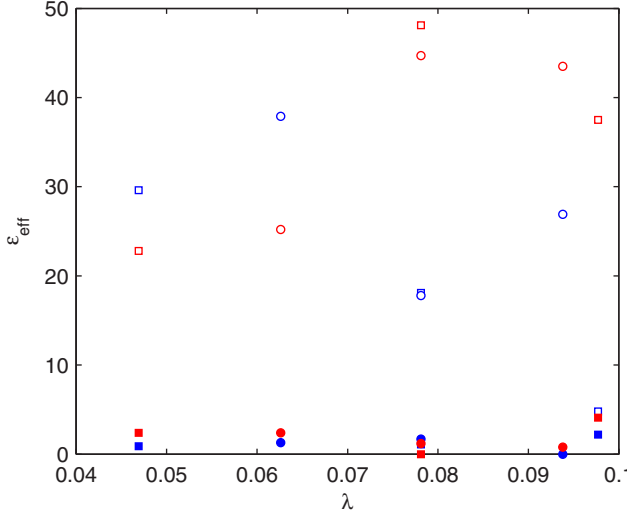


FIG. 13. The effective static contact angle difference of droplets on rough hydrophobic and hydrophilic surfaces. Red: hydrophilic; blue: hydrophobic; square: rectangular surface; circle: sinusoidal surface; solid: dual surface; empty: nondual surface.

sinusoidal rough surfaces are extended in the z direction parallel to grooves, and pinned at sharp groove edges only in the x direction, so their θ_{eff}^x are larger than θ_{eff}^z , and ε_{eff} may achieve 50°. Elevated blocks on dual-rectangular and dual-sinusoidal surfaces pose an energy barrier [27,28] hindering the extension of droplets in both directions, so that droplets are pinned in the x and z directions, and $\theta_{\text{eff}}^{x,z}$ is much larger than the corresponding θ_0 on a smooth surface, while ε_{eff} remains less than 5°.

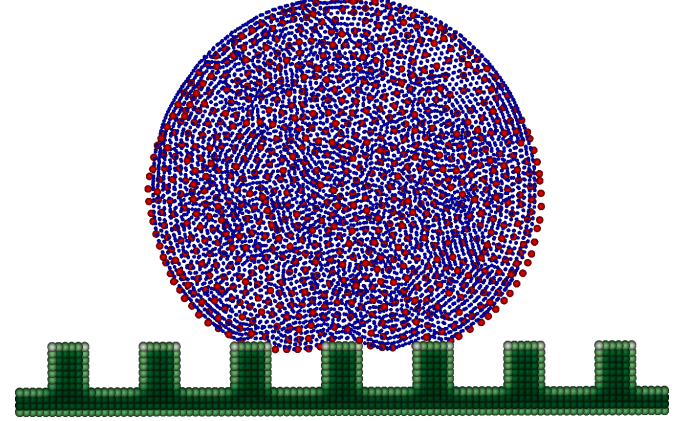


FIG. 14. Comparison of effective contact angles on a fine-roughness dual-rectangular surface obtained from a high-resolution (particle spacing 2.5×10^{-5} mm; $\theta_{\text{eff}}^x = 149.36^\circ$; $\theta_{\text{eff}}^z = 150.28^\circ$) and a low-resolution (particle spacing 5×10^{-5} mm; $\theta_{\text{eff}}^x = 151.52^\circ$; $\theta_{\text{eff}}^z = 150.84^\circ$) simulation. Green particles: solid surface; red particles: low resolution; blue particles: high resolution.

VIII. THE EFFECT OF RESOLUTION ON EFFECTIVE STATIC CONTACT ANGLE

To study the effect of resolution on PF-SPH solutions, we compare static contact angles of droplets on a fine dual-rectangular-type surface obtained from PF-SPH simulations with two different resolutions. In the high-resolution simulation, the number of particles is eight times higher than the number of particles in the low-resolution simulation. The particle spacing in the high-resolution simulation is 2.5×10^{-5} mm, the smoothing length is $h = 8.55 \times 10^{-5}$ m,

TABLE III. Effective static contact angles of droplets with R_0 ranging from 0.5 to 1.6 mm on fine-, medium-, and coarse-roughness dual-rectangular hydrophobic surfaces.

R_0 (mm)	0.5	0.6	0.7	0.8	0.9	1.0	1.1	1.2	1.4	1.6
R_{eq} (mm)	0.44	0.54	0.64	0.73	0.83	0.92	1.02	1.11	1.3	1.5
ΔP (Pa)	330.68	269.33	227.34	199.32	175.3	158.15	142.65	131.08	111.92	97.00
Fine roughness										
p_c (Pa)	235.81									
θ_{eff}^x	122.8°	135.7°	123.7°	151.5°	133.6°	139.3°	142.1°	129.8°	136.2°	126.1°
θ_{eff}^z	124.1°	137.9°	122.7°	150.6°	135.2°	140.7°	143.4°	136.8°	136.7°	126.2°
ε_{eff}	1.3°	2.2°	1.0°	0.1°	1.6°	1.4°	1.3°	7.0°	0.5°	0.1°
Medium roughness										
p_c (Pa)	193.49									
θ_{eff}^x	123.4°	135.2°	142.7°	135.5°	139.5°	129.5°	129.1°	137.4°	135.6°	132.8°
θ_{eff}^z	124.1°	124.3°	138.4°	136.6°	131.7°	129.4°	131.2°	126.6°	137.7°	137.2°
ε_{eff}	0.7°	10.9°	4.3°	1.1°	7.8°	0.1°	2.1°	0.8°	2.2°	4.4°
Coarse roughness										
p_c (Pa)	209.61									
θ_{eff}^x	120.6°	125.6°	136.6°	125.9°	130.8°	140.7°	146.4°	135.2°	128.9°	135.8°
θ_{eff}^z	135.3°	125.0°	139.0°	128.1°	133.5°	126.7°	141.1°	130.4°	141.7°	126.6°
ε_{eff}	14.7°	0.6°	3.4°	2.2°	2.7°	14.0°	5.3°	4.8°	12.8°	9.2°

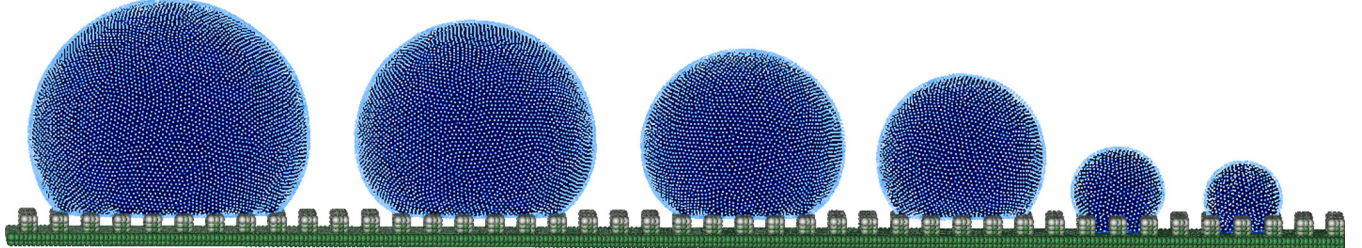


FIG. 15. Droplets on a fine-roughness dual-rectangular surface. Equilibrated radii of droplets are 1.5, 1.3, 1.11, 0.92, 0.54, and 0.44 mm.

the mass m of each particle is 1.5625×10^{-11} kg, the speed of sound c is 4.5 m/s, and the surface tension of water is achieved with a fluid-fluid interaction strength $s_{ff} = 1.9 \times 10^{-6}$. The low-resolution simulation has the same parameters as the simulations in the preceding sections.

Figure 14 shows the static contact angles obtained from the simulations with these two resolutions. The angles θ_{eff}^x and θ_{eff}^z are nearly the same in both simulations.

IX. TRANSITIONS BETWEEN CASSIE AND WENZEL STATES

Here, we simulate ten liquid droplets with initial radii ranging from 0.5 to 1.6 mm, which are brought into contact with fine-roughness ($d = 0.2$ mm; $l = 0.15$ mm), medium-roughness ($d = 0.25$ mm; $l = 0.2$ mm), and coarse-roughness ($d = 0.25$ mm; $l = 0.25$ mm) dual-rectangular hydrophobic surfaces. The effective contact angles of these droplets are listed in Table III. Figure 15 demonstrates six liquid droplets on a fine-roughness dual-rectangular surface.

All droplets on rough surfaces create unique shapes depending on the number of blocks they touch, so their $\theta_{\text{eff}}^{x,z}$ values vary in the range from 120.6° to 151.5° , and ϵ_{eff} varies in the range from 0.1° to 14° . The variation in $\theta_{\text{eff}}^{x,z}$ for different droplet sizes can be explained by the Gibbs criterion [28], which attributes the pinning effects of the liquid-air interface to sharp edges of the solid surface. In our simulations, for two different-size droplets placed on equal number of blocks (droplets with $R_{\text{eq}} = 1.11$ and 1.3 mm in Fig. 16), the larger droplet creates larger $\theta_{\text{eff}}^{x,z}$, because it is pinned by the edge of the block. A further increase of the droplet size (the droplet

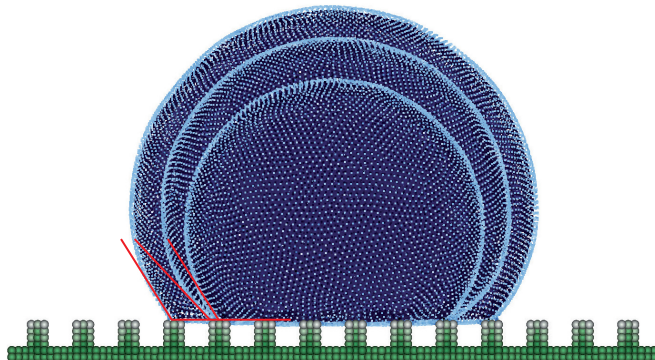


FIG. 16. Pinning effect of droplets on a fine-roughness dual-rectangular surface. Equilibrated radii of droplets are 1.11, 1.3, and 1.5 mm.

with $R_{\text{eq}} = 1.5$ mm in Fig. 16) leads to an immediate jump to the next block and decrease of $\theta_{\text{eff}}^{x,z}$.

We observe a transition between Wenzel and Cassie regimes based on droplet size (Figs. 15 and 17). Droplets with $R_{\text{eq}} > 0.64$ mm on a fine-roughness dual-rectangular surface remain in the Cassie regime; droplets with $R_{\text{eq}} \leq 0.64$ mm are in a Wenzel state. Various authors [e.g., 29–31] have investigated this transition phenomenon in terms of critical capillary pressure p_c :

$$p_c = -\frac{\sigma f \cos(\theta_0)}{(1-f)L}, \quad (30)$$

where σ is the water surface tension, θ_0 is the corresponding static contact angle of a droplet on a flat hydrophobic surface, and f is a fraction of the wetted projection area, where $L = l/4$ and $f = l^2/(l+d)^2$. Here l and d are the surface parameters as described in the previous chapters.

A Cassie-to-Wenzel transition occurs if the pressure inside the droplet, ΔP , becomes larger than p_c , where ΔP can be found from the Young-Laplace law:

$$\Delta P = \frac{2\sigma}{R_{\text{eq}}}. \quad (31)$$

For a fine-roughness dual-rectangular surface and the given fluid configuration, droplets switch from a Cassie to a Wenzel

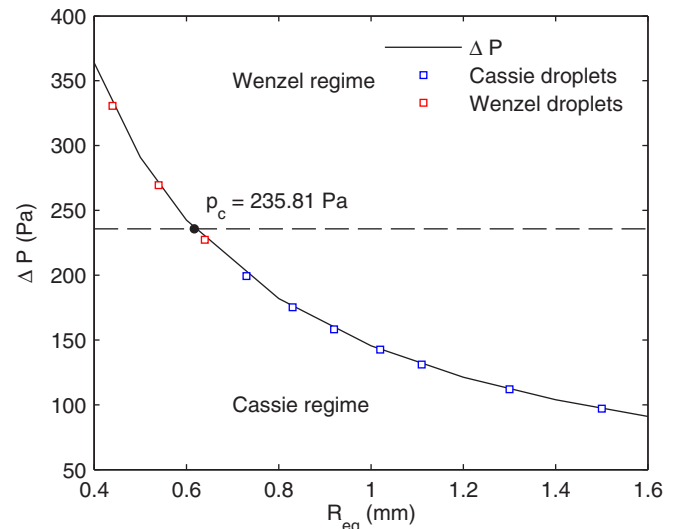


FIG. 17. Cassie-to-Wenzel transition based on critical capillary pressure and internal pressures of droplets with R_{eq} ranging from 0.44 to 1.5 mm for a fine-roughness dual-rectangular surface.

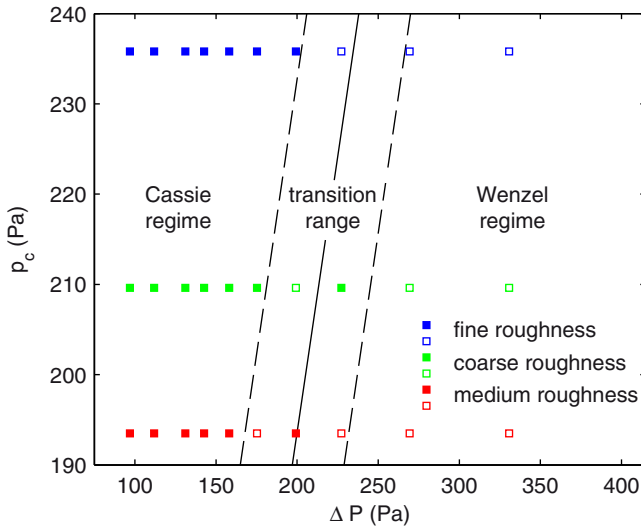


FIG. 18. Cassie-to-Wenzel transition based on critical capillary pressures and internal pressures of droplets ranging from 97.00 to 330.68 Pa (corresponding R_{eq} are ranging from 1.5 to 0.44 mm) for fine-, medium-, and coarse-roughness dual-rectangular surfaces. Open symbols: Wenzel regime; filled symbols: Cassie regime.

state when $\Delta P > p_c$ ($p_c = 235.81 \text{ Pa}$) at a radius $R_{\text{eq}} < 0.62 \text{ mm}$ (Fig. 17).

Some droplets with a value ΔP close to the theoretical value p_c (like a droplet with $R_{\text{eq}} = 0.64 \text{ mm}$ in Fig. 17) can be in both Cassie and Wenzel states, such that no clear transition point can be detected. Instead we define a transition region for droplets with $\Delta P = p_c \pm 30 \text{ Pa}$ which can be in both states (Fig. 18) based on our simulation results. A region between two dashed lines in Fig. 18 represents the region at which the Cassie-to-Wenzel transition occurs for all types of dual rectangular surfaces. All large droplets with $R_{\text{eq}} \geq 0.92 \text{ mm}$ ($\Delta P \leq 158.15 \text{ Pa}$) are in a Cassie state, while small droplets with $R_{\text{eq}} \leq 0.64 \text{ mm}$ ($\Delta P \geq 227.34 \text{ Pa}$) are in a Wenzel state. The width of the transition region may depend on resolution

effects or pressure fluctuations during the equilibration of droplets on the surface.

Next, we investigate the dependence of droplet state on initial conditions. We simulate droplets with $R_{\text{eq}} = 0.64$ and 1.3 mm , which are brought into contact with a fine-roughness dual-rectangular surface. In the first case, the droplet center is located between two rectangular blocks [left droplets in Figs. 19(a) and 19(c)]; for the second case, the droplet center is located above the center of a rectangular block [right droplets in Figs. 19(a) and 19(c)]. For both cases the droplet state remains the same, independent on initial placement relative to the surface roughness. The small droplet stays in a Wenzel state, and the large one in a Cassie state. This difference is caused by the initial placement of droplets relative to the roughness, which influences the effective static contact angle due to pinning effects (Table IV). A small droplet with a center located above a block has a larger effective contact angle. For the large droplet the effective contact angle is larger if the droplet center is located between blocks.

Figures 19(b) and 19(d) show droplets with $R_{\text{eq}} = 0.64$ and 1.3 mm , dropped from 1.75 mm height (measured between surface and droplet center). Small droplets with $R_{\text{eq}} = 0.64 \text{ mm}$ stay in a Wenzel state [Fig. 19(b)], while large droplets with $R_{\text{eq}} = 1.3 \text{ mm}$ turn from a Cassie to Wenzel state [Fig. 19(d)] due to additional pressure caused by gravitational impact. Therefore, the initial height from which droplets are dropped influences the effective contact angle hysteresis. Both small and large droplets dropped from 1.75 mm height have smaller effective contact angles than droplets placed directly above a surface.

X. DROPLET FLOW ON ROUGH SURFACES

In this section, we study droplet flow on rough surfaces with a surface inclination angle α ranging from 10° to 90° . We create two types of rough surfaces: a surface with rectangular bars oriented parallel to the flow direction and one with rectangular bars oriented perpendicular to the flow direction. For comparison, we also simulate flow on smooth surfaces. We

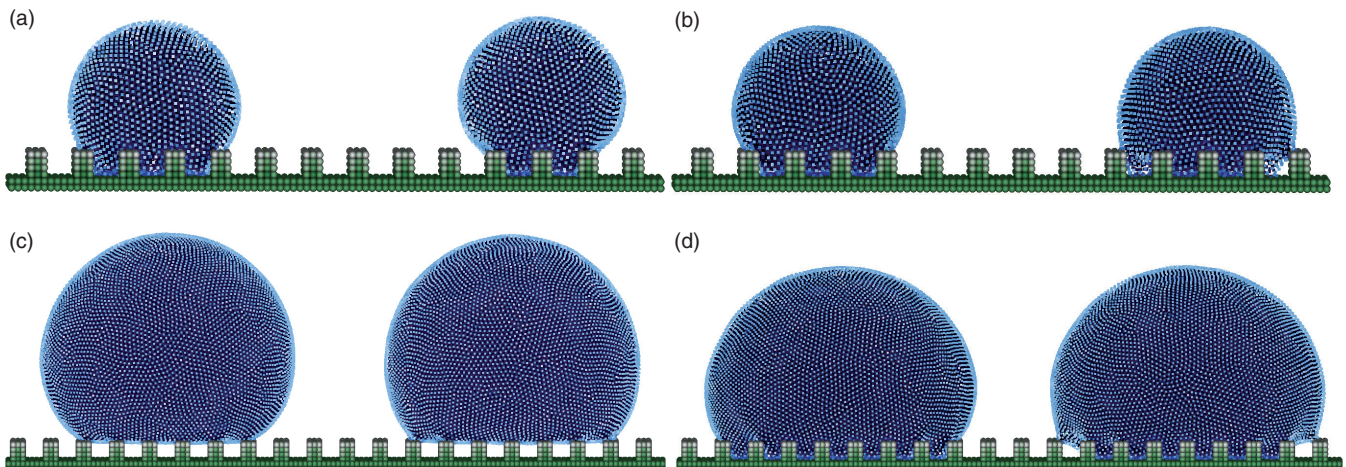


FIG. 19. Droplet states depending on initial conditions: (a) droplets with $R_{\text{eq}} = 0.64 \text{ mm}$ are brought into contact with a rough surface; (b) droplets with $R_{\text{eq}} = 0.64 \text{ mm}$ are dropped from 1.3 mm height; (c) droplets with $R_{\text{eq}} = 1.3 \text{ mm}$ are brought into contact with a rough surface; (d) droplets with $R_{\text{eq}} = 1.3 \text{ mm}$ are dropped from 1.75 mm height.

TABLE IV. Effective static contact angles of droplets with $R_{\text{eq}} = 0.64$ and 1.3 mm on a fine-roughness dual-rectangular hydrophobic surface depending on initial conditions.

Mode of placement	$R_{\text{eq}} = 0.64$ mm				$R_{\text{eq}} = 1.3$ mm			
	Immediate contact ^a		Dropped ^b		Immediate contact		Dropped	
Droplet position	Pit centered	Block centered	Pit centered	Block centered	Pit centered	Block centered	Pit centered	Block centered
θ_{eff}^x	121.7°	138.4°	118.7°	113.3°	137.9°	129.5°	118.8°	113.3°
θ_{eff}^z	122.1°	137.9°	119.1°	113.5°	138.2°	130.4°	118.4°	113.8°
ε_{eff}	0.4°	0.5°	0.4°	0.2°	0.3°	0.9°	0.4°	0.5°

^aEquilibrated in contact with the surface.

^bDropped from 1.75 mm height.

simulate flow of two different states: flow of Cassie droplets on microscopically hydrophobic surfaces (with $\theta_0 = 122.7^\circ$ corresponding to $s_{\text{sf}} = 0$), and flow of Wenzel droplets on microscopically hydrophilic surfaces (with $\theta_0 = 84.7^\circ$ corresponding to $s_{\text{sf}} = 1.3 \times 10^{-6}$). In these simulations, a droplet is discretized with 195 216 fluid particles and the surface with approximately 235 000 solid particles. The simulations are run on 32 cores.

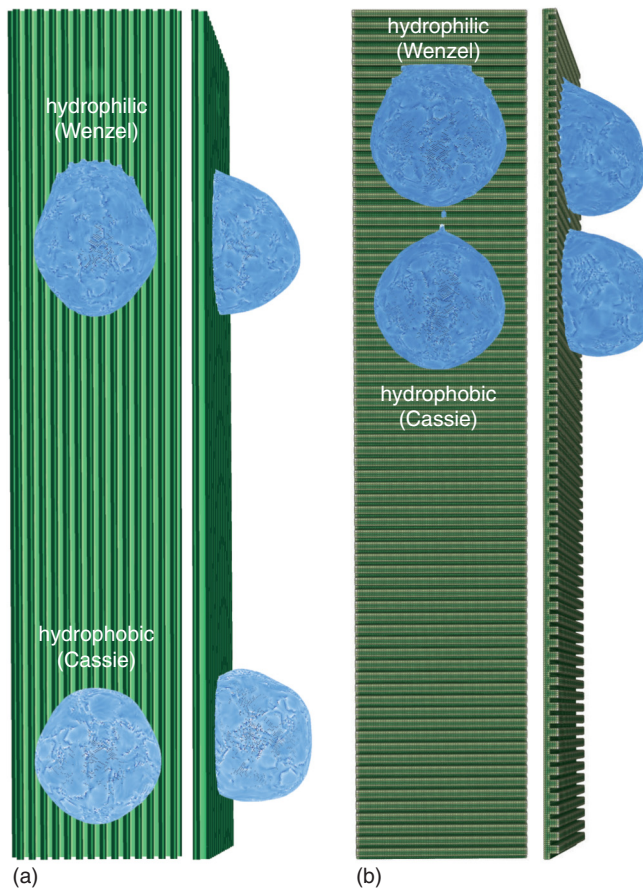


FIG. 20. Hydrophobic and hydrophilic droplets flowing on a rough rectangular surface with rectangular bars oriented parallel to the flow direction (a) and rectangular bars oriented perpendicular to the flow direction (b) at the time step $t = 50\,000$ (46.296 ms). Surface inclination angle is $\alpha = 90^\circ$.

Figure 20 shows simulation results for Cassie and Wenzel droplet flows on these rough surfaces with $\alpha = 90^\circ$ after 50 000 time steps ($t = 46.296$ ms). Cassie and Wenzel droplets can easily slide along the rough surface with inclination angles α ranging from 10° to 90° if rectangular bars are oriented parallel to the flow direction. However, if rectangular bars are oriented perpendicular to the flow direction, a Cassie droplet barely moves and a Wenzel droplet remains stationary for all surface inclination angles α . These results show a good qualitative agreement with experimental results of [9].

Next, we investigate the relationship between Bo and Ca numbers observed in our simulations. It was shown by Podgorski *et al.* [15] that droplet dynamics on smooth surfaces follows the linear scaling law:

$$\text{Ca} = \gamma \text{Bo} \sin(\alpha) - \Delta_\theta, \quad (32)$$

where the Ca number is defined as

$$\text{Ca} = \mu v / \sigma, \quad (33)$$

and the Bo number as

$$\text{Bo} = \frac{\rho g V^{2/3}}{\sigma}. \quad (34)$$

Here, v is the droplet velocity, V the equilibrium droplet volume, α the surface inclination angle measured from the horizontal, Δ_θ is a perimeter-averaged projection factor of the surface tension, and γ a constant related to the specific fluid-solid combination. The linear dependence between Ca and Bo for droplet flow on smooth surfaces was numerically confirmed by Kordilla *et al.* [17] via PF-SPH simulations for a range of wetting conditions; however, it has not been shown to hold for rough surfaces.

The results of our simulations, plotted in Fig. 21, demonstrate an existing linear relationship between Ca and Bo numbers for $\text{Bo} \sin \alpha < 1$. For higher values of $\text{Bo} \sin \alpha$, the relationship becomes nonlinear. A similar transition from linear to nonlinear behavior for droplets on smooth surfaces has been reported in Kordilla *et al.* [17] and Podgorski *et al.* [15], which is mainly caused by the deviation of droplet shapes from the spherical cap form.

Our results show that Cassie droplets on a rough surface with parallel orientation of bars to the flow direction move approximately 1.2 times faster than droplets on a smooth surface with the same θ_0 and α . On the other hand, Wenzel droplets on a surface with the same roughness move 1.8 times

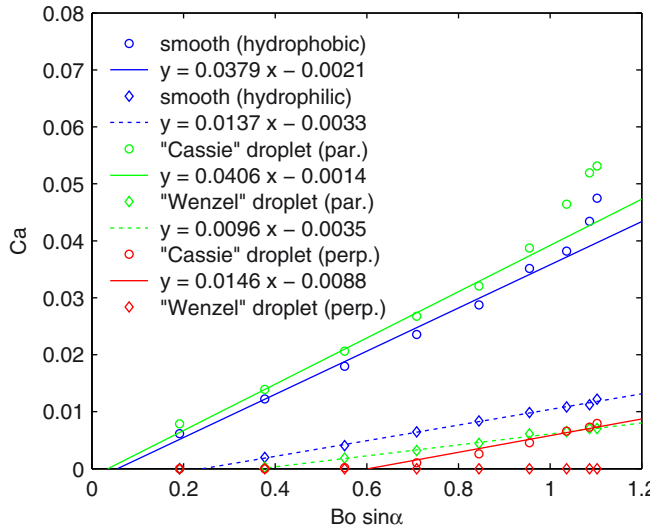


FIG. 21. Dimensionless scaling for smooth and rough hydrophobic and hydrophilic surfaces with different orientations of roughness relative to the droplet flow direction. (par.): flow parallel to the orientation of the bars; (perp.): flow perpendicular to the orientation of bars. The surface inclination angles α are $10^\circ, 20^\circ, 30^\circ, 40^\circ, 50^\circ, 60^\circ, 70^\circ, 80^\circ$, and 90° .

slower than a droplet on a smooth surface with the same θ_0 and α . Cassie droplets on the rough surface with bars perpendicular to flow do not start moving until $Bo \sin \alpha \approx 0.6$. For larger $Bo \sin \alpha$, Cassie droplets accelerate faster than droplets on a smooth surface with the same θ_0 . Wenzel droplets on the rough surface with “perpendicular bars” remain immobile for all considered $Bo \sin \alpha$.

XI. CONCLUSION

We employed a three-dimensional PF-SPH model to simulate static and dynamic droplets on rough hydrophobic and hydrophilic surfaces. We demonstrate that PF-SPH can model flow under various wetting conditions. We also validated the model against several analytical solutions and performed a convergence study.

In PF-SPH, the surface tension and microscopic static contact angle θ_0 result from pairwise forces added into the SPH momentum conservation equation. In this work, we chose the pairwise forces to cover a wide range of microscopic static contact angles. We simulated droplets and measured effective static contact angles θ_{eff} on surfaces with different types of surface roughness, including rectangular, dual-rectangular, sinusoidal, and dual-sinusoidal. For each type of surface geometry, we considered microscale hydrophobic and hydrophilic surfaces with different degrees of roughness, including fine, medium, and coarse.

We observed that Cassie droplets form on microscopically hydrophobic surfaces, and Wenzel droplets form on hydrophilic surfaces. We studied the dependence of θ_{eff} on the

degree of roughness, characterized by a dimensionless ratio λ , with larger λ corresponding to coarser surface roughness relative to the droplet size. The effective static contact angle of Cassie droplets decreases with increasing λ . The effective contact angle of Wenzel droplets may increase or decrease with increasing λ , which is attributed to the existence of pinning effects. For most studied rough surfaces, we found θ_{eff} to be greater than θ_0 . Our results showed that roughness can cause microscopically hydrophilic surfaces to behave as macroscopically hydrophobic. Moreover, microscopically hydrophilic surfaces showed even stronger macroscopic hydrophobic behavior.

In order to investigate the transition between the Cassie and Wenzel regimes we simulated liquid droplets with initial radii ranging from 0.5 to 1.6 mm on dual-rectangular hydrophobic surfaces and compare our results to theoretical predictions. Good agreement is found between the analytical solution and PF-SPH simulations. However, depending on size and internal pressure, a transition region exists where droplets may stay in a Cassie or Wenzel state. This behavior is shown to depend on initial conditions, in terms of lateral droplet position relative to the roughness and initial height. Both parameters control the hysteresis of dynamic contact angles due to pinning effects and are also present in our simulations, due to the rather coarse roughness of the surfaces relative to droplet size.

Finally, we studied droplet flow on inclined rough and smooth surfaces. We demonstrated that the type and degree of roughness, as well as the orientation of surface features relative to flow, significantly affect droplet dynamics. If rectangular bars are oriented parallel to the flow direction, water droplets can easily slide on rough hydrophobic and hydrophilic surfaces. On the other hand, if rectangular bars are oriented perpendicular to the flow direction, droplets barely move on hydrophobic surfaces and remain stationary on hydrophilic surfaces for all surface inclination angles. We demonstrated numerically that the linear scaling between the Bond and capillary numbers described in Podgorski *et al.* [15] is valid not only for sliding droplets on smooth surfaces, but also for sliding droplets on rough hydrophobic and hydrophilic surfaces. The presented simulations covered a wide spectrum of wetting conditions and types of surface roughness. The influence of surface roughness and orientation on flow dynamics in the case of more complex flow regimes, such as rivulets and stable and unstable films, is part of future work.

ACKNOWLEDGMENTS

This work was funded by the Deutsche Forschungsgemeinschaft (DFG; German Research Foundation) under Grants No. SA 501/26-1 and No. KO 5359/1-1. E.S. was partially supported by the DAAD (German Academic Exchange Service). A.M.T. was supported by the Department of Energy (DOE)'s Office of Advanced Scientific Computing Research and Pacific Northwest National Laboratory (PNNL). PNNL is operated by Battelle for the DOE under Contract No. DE-AC05-76RL01830.

[1] D. Quéré, P. de Gennes, F. Brochard-Wyart, and A. Reisinger, *Capillarity and Wetting Phenomena: Drops, Bubbles, Pearls, Waves* (Springer Science & Business Media, Berlin, 2004).

[2] J. Genzer and K. Efimenko, *Biofouling* **22**, 339 (2006).

[3] D. Voigt and S. Gorb, *Proc. R. Soc. B* **277**, 895 (2010).

[4] Y. Zhao, Q. Lu, M. Li, and X. Li, *Langmuir* **23**, 6212 (2007).

- [5] C. Yang, U. Tartaglino, and B. Persson, *Eur. Phys. J. E* **25**, 139 (2008).
- [6] C. D. Daub, J. Wang, S. Kudesia, D. Bratko, and A. Luzar, *Faraday Discuss.* **146**, 67 (2010).
- [7] J. J. Huang, C. Shu, and Y. T. Chew, *Phys. Fluids* **21**, 022103 (2009).
- [8] D. Byun, J. Kim, H. S. Ko, and H. C. Park, *Phys. Fluids* **20**, 113601 (2008).
- [9] P. Zhang, H. Liu, J. Meng, G. Yang, X. Liu, S. Wang, and L. Jiang, *Adv. Mater.* **26**, 3131 (2014).
- [10] C. Stamatopoulos, T. M. Schutzius, C. J. Köppl, N. El Hayek, T. Maitra, J. Hemrle, and D. Poulikakos, *Sci. Rep.* **6**, 18875 (2016).
- [11] S. Plimpton, *Comput. Phys.* **117**, 1 (1995).
- [12] A. M. Tartakovsky and A. Panchenko, *J. Comput. Phys.* **305**, 1119 (2016).
- [13] O. Voinov, *Fluid Dyn.* **11**, 714 (1976).
- [14] L. Tanner, *J. Phys. D: Appl. Phys.* **12**, 1473 (1979).
- [15] T. Podgorski, J.-M. Flesselles, and L. Limat, *Phys. Rev. Lett.* **87**, 036102 (2001).
- [16] A. Tartakovsky and P. Meakin, *Phys. Rev. E* **72**, 026301 (2005).
- [17] J. Kordilla, A. M. Tartakovsky, and T. Geyer, *Adv. Water Resour.* **59**, 1 (2013).
- [18] H. Wendland, *Adv. Comput. Math.* **4**, 389 (1995).
- [19] G. K. Batchelor, *An Introduction to Fluid Dynamics* (Cambridge University Press, Cambridge, UK, 1967).
- [20] J. J. Monaghan, *Rep. Prog. Phys.* **68**, 1703 (2005).
- [21] J. P. Morris, P. J. Fox, and Y. Zhu, *J. Comput. Phys.* **136**, 214 (1997).
- [22] M. P. Allen and D. J. Tildesley, *Computer Simulation of Liquids* (Oxford University Press, New York, 1989).
- [23] A. M. Tartakovsky and P. Meakin, *Vadose Zone J.* **4**, 848 (2005).
- [24] D. Bonn, J. Eggers, J. Indekeu, J. Meunier, and E. Rolley, *Rev. Mod. Phys.* **81**, 739 (2009).
- [25] R. N. Wenzel, *Ind. Eng. Chem.* **28**, 988 (1936).
- [26] A. Cassie and S. Baxter, *Trans. Faraday Soc.* **40**, 546 (1944).
- [27] Y. Tsoumpas, S. Dehaeck, M. Galvagno, A. Rednikov, H. Ottevaere, U. Thiele, and P. Colinet, *Langmuir* **30**, 11847 (2014).
- [28] J. W. Gibbs, *Scientific Papers* (Longmans, London, 1906).
- [29] Q.-S. Zheng, Y. Yu, and Z.-H. Zhao, *Langmuir* **21**, 12207 (2005).
- [30] C. Dorrer and J. Rühe, *Soft Matter* **5**, 51 (2009).
- [31] C. Dorrer and J. Rühe, *Langmuir* **23**, 3820 (2007).